

# Improved predictability of forming limit curves through microstructural inputs

S. K. Mishra · Sharvari G. Desai · Prita Pant ·  
K. Narasimhan · I. Samajdar

Received: 5 August 2008 / Accepted: 7 January 2009 / Published online: 27 January 2009  
© Springer/ESAFORM 2009

**Abstract** Forming Limit Curves (FLCs) were determined experimentally through limiting dome height (LDH) tests in AA1050, AISI 316L and AISI 304L. FLCs were also simulated through FE (finite element) analysis. Simulations involved both constant and varying (with strain and strain path) material properties — namely, strain hardening exponent ( $n$ ) and normal anisotropy ( $\bar{r}$ ). Varying  $n$  values were estimated from limited experimental data (from tensile tests) and the implicit assumption that  $n$  scales with in-grain misorientation developments and formation of strain induced martensite.  $\bar{r}$ , on the other hand, could be estimated from crystallographic texture only for AA1050. Simulations with varying  $\bar{r}$  in AA1050 had shown a clear, though numerically marginal, improvement. On the other hand, varying  $n$  could remarkably improve the FLC predictability in 316L and 304L, especially in the biaxial region.

**Keywords** Formability · Forming limit curve · Finite element analysis · Texture · Microstructure · Strain hardening exponent · Strain induced martensite · In-grain misorientation

## Introduction

Sheet metal forming finds a wide range of applications in modern technological society. Such applications demand in-depth understanding, both scientific and applied, of sheet metal formability. The latter is often popularly represented as forming limit curves (FLCs) [1–3]. An FLC is generated by deforming material at different strain-paths and then plotting a boundary demarcating necked samples, the implicit assumption being that materials do not fail below FLC and are safe to form, if wrinkling is avoided [1–4].

Experimental measurement of FLCs is both expensive and time consuming. Therefore, it is useful to predict the FLCs. Advanced finite element (FE) packages [5–11] and availability of accurate material models [10–21] has made simulations of even most complex geometries [22, 23] a practical choice for today's metal forming industries. The quest for better forming predictability is an area of significant technological importance [24–25]. But this is also an area where the science of microstructures finds limited usage. For example, it is normally understood [26–30] that variations in important material properties (of relevance to FE simulations are strain hardening exponent ( $n$ ) and normal anisotropy ( $\bar{r}$ )) during forming can affect the forming behavior and the forming limits. However, such variations are rarely taken into account in FLC simulations. In the present work the variations in strain hardening exponent and normal anisotropy as a function of strain and strain path are incorporated while simulating the FLC.

Three fcc metals were selected for this study: AA1050, AISI 316L and AISI 304L. It may be noted that the selected

---

S. K. Mishra · P. Pant · K. Narasimhan (✉) · I. Samajdar  
Department of Metallurgical Engineering and Material Sciences,  
Indian Institute of Technology,  
Mumbai, India  
e-mail: nara@iitb.ac.in

S. G. Desai  
Department of Mechanical Engineering,  
Indian Institute of Technology,  
Bombay, India

metals have a range of material properties<sup>1</sup> and were observed (and are expected) [31–38] to have remarkably different microstructural developments. Some earlier studies [31–32] have already shown improvement in FLC prediction by using materials model which takes into account changes in material properties during deformation. The objective of the present study is to use microstructural developments, in terms of changing material properties ( $\bar{r}$  &  $n$ ), as inputs towards FLC simulations.

## Experimental details

### Material and deformation

In this study fully annealed commercial AA1050, AISI 316L and AISI 304L (chemical compositions are listed in Table 1 and 2) sheets of about 1 mm thickness were used. The mechanical properties of these materials were measured through standard tensile and  $\bar{r}$  bar tests — ASTM E 8M & ASTM E 517 respectively. The use of an extensometer ascertained reasonable accuracy in strain measurement. 2.5 mm screen printed circular grids were used for estimation of effective strain in deformed samples. Table 3 lists the starting properties which are needed for subsequent FE analysis of the three materials and Barlat's parameters [39] for FE analysis of AA1050. The sheets were also subjected to limiting dome height (LDH) [25] tests in a 200 ton double-action hydraulic press. To achieve different strains-paths, different sheet geometries [3] were used. After deformation, strain and strain-paths were estimated using the standard [1–4] procedure and the experimental FLCs were obtained.

Three different strains and strain-paths were selected for subsequent microstructural characterization. Strains were classified as low (LS), intermediate (IS) and high (HS), while strain-paths were generalized as biaxial (BS), uniaxial (US) and plane strain (PS) (see Table 4). Table 4 also lists effective strain values ( $\bar{\epsilon}$ ) calculated for the three materials using the Hill's 48 yield function [16] and the equation for calculating the effective strain is given in eq. (1). The effective strain estimates offer a common basis for comparison between the different strain-paths.

$$\bar{\epsilon} = \frac{1 + \bar{r}}{1 + 2\bar{r}} \left[ \epsilon_1^2 + \epsilon_2^2 + \left( \frac{2\bar{r}}{1 + \bar{r}} \right) \epsilon_1 \epsilon_2 \right]^{\frac{1}{2}} \quad (1)$$

<sup>1</sup> Of specific interest, from the point of microstructural developments, are the stacking fault energy values. These are about 175, 60 and 20 J/m<sup>2</sup> respectively for AA1050, 316L and 304L.

**Table 1** Chemical compositions, in wt% alloying elements, of AA1050

Material	Fe	Cu	Zn	Mn	Ti	Si	Mg	Al
AA1050	0.4	0.005	0.007	0.05	0.003	0.08	0.004	Bal.

Where  $\bar{r}$  is the average plastic anisotropy,  $\epsilon_1$  and  $\epsilon_2$  are the major and minor true strain respectively.

### Microstructural characterization

#### X-ray diffraction

Bulk texture measurements were obtained using a Panalytical MRD System for the selected samples (as given in Table 4). Orientation Distribution Functions (ODFs) were measured by the inversion of four incomplete pole figures and using the program MTM-FHM [40]. FHM represents fast harmonic measurements and uses standard series expansion [41]. In the present study, the X-ray ODFs were used for calculating texture estimated  $\bar{r}$  [40] for AA 1050<sup>2</sup> and Texture Index (TI) for all the materials. From bulk texture measurements  $r$  values (normal anisotropy values) were estimated using MTM-FHM program and the methodology described elsewhere [42]. Texture index, or  $\int [f'(g)]^2 dg$ , where  $f(g)$  is the ODF intensity [43], can be used to represent the relative texturing or anisotropy. From the measured XRD (X-ray diffraction) patterns, the percentage of bcc martensite phase was also estimated for AISI 316L and 304L. Martensite percentage was estimated [44] from X-ray diffraction data using equation

$$V_{\alpha'} = \frac{\sum_0^n (I_{\alpha'}^{hkl} / R_{\alpha'}^{hkl})}{\sum_0^n (I_{\alpha'}^{hkl} / R_{\alpha'}^{hkl}) + \sum (I_{\gamma}^{hkl} / R_{\gamma}^{hkl})} \quad (2)$$

Where  $\alpha'$  and  $\gamma$  are related respectively to the martensite and austenitic phase

$I_{\alpha'}^{hkl}$  is the corrected integrated intensity of diffraction line (hkl)

$R^{hkl}$  is the corresponding theoretical line intensity,

$$R^{hkl} = \frac{1}{V^2} \left[ |FF^*| \times e^{-2M} \right]$$

$|FF^*|$  the structure factor times its complex conjugate

$e^{-2M}$  the Debye - Waller or temperature factor

$V$  the unit cell volume of the diffracting phase

<sup>2</sup> It needs to be stated, at this stage, that presence of significant twinning and strain induced martensite in 316L and 304L makes any  $\bar{r}$  estimates from crystallographic texture meaningless in these two materials.

**Table 2** Chemical compositions, in wt% alloying elements, of AISI 316L & 304L

Material	C	Mn	P	S	Si	Cr	Ni	Mo	Cu	Al	Fe
AISI 316L	0.025	1.24	0.0323	0.0125	0.309	17.07	10.44	2.08	0.42	0.0202	Bal.
AISI 304L	0.02	1.63	0.003	0.005	0.40	18.20	9.55	0.03	0.03	0.011	Bal.

### Electron back scattered diffraction (EBSD)

EBSD samples were prepared using the standard electro-polishing technique [38, 45]. A TSL-EDX OIM (orientation imaging microscopy) or EBSD system on an FEI Quanta 200HV SEM (scanning electron microscope) was used. For each sample, an area of more than 2 mm<sup>2</sup> was scanned with step sizes of 0.3 μm or lower. The present study used EBSD scans for two purposes: for estimating the percentage of strain induced martensite<sup>3</sup> and in-grain misorientations. For the latter, grain average misorientation (GAM) values were used. Grains were identified from the presence of continuous boundaries of above 1° misorientation; GAM values were then estimated as average point-to-point misorientation within a grain.

### Finite element analysis

LDH (limiting dome height) tests were simulated using finite element (FE) analysis software PAMSTAMP 2G. Simulations were conducted for different strain-paths using appropriate boundary conditions. For the simulations, different yield criteria were tried out. Barlat's and Hill's Yield criterion emerged as the best respectively for aluminum (AA1050) (as shown in Fig. 1a) and austenitic stainless steel (316L & 304L). These were used, in the present study, for both constant and varying material properties (e.g.  $n$  and  $\bar{r}$ ). To represent stress-strain relation the Holloman hardening law was used and a friction coefficient of 0.12 (between punch and blank) was assumed. For simulations with varying material properties,  $n$  and  $\bar{r}$  were changed in different strain-paths at an increment of 0.1 effective strain. A localized neck can be perceived by the presence of a critical local thickness gradient. Such a perception is independent of the strain path, rate of forming and material properties. In the M-K type analysis [46], the above concept implies that necking should be predicted when the ratio of the thickness of the notch to that of the bulk drops below a critical magnitude  $R_{cri}$ .

$$f = \frac{\text{current thickness notch}}{\text{current thickness of bulk}} \leq R_{cri} \quad (3)$$

<sup>3</sup> These were confirmed by X-ray diffraction (valid for higher martensite percentages) and VSM (vibrating sample magnetometer) [34].

In the present simulations, evolution of thickness ratio (equivalent of  $f$ ) between neighboring finite elements was monitored and necking was predicted when it drops below  $R_{cri}$ . The magnitude of  $R_{cri}$  was earlier established as equal to 0.92 by careful experimentation [47, 48].

## Results

### FLCs using constant material parameters

As shown in Fig. 1, FLC predictions assuming constant  $n$  and  $\bar{r}$  brought different degrees of success. In AA1050 (Fig. 1a) the FLC predictions using Barlat's 1991 [39] and Hill's 48 [16] yield functions were compared with the experimental plot. The former showed a better comparison with the experimental plot. For 316L and 304L the FLC predictions using Hill's 48 [16] yield function were compared with the experimental plot and the differences between predicted and experimental plot were significant.

**Table 3** Mechanical properties of the three materials

Direction	YS (Mpa)	UTS (Mpa)	Elongation (%)	$n$	$K$	$r$	$\bar{r}$	$\Delta r$
<b>AA1050</b>								
0°	70	91	38	0.24	145	0.69	0.77	-0.02
90°	68	89	48	0.25	148	0.83		
45°	65	83	49	0.23	150	0.79		
<b>AISI 316L</b>								
0°	637	303	71	0.37	1228	0.84	1.13	-0.12
90°	624	300	66	0.32	1210	1.30		
45°	630	296	60	0.31	1190	1.20		
<b>AISI 304L</b>								
0°	705	254	69	0.39	1309	0.89	1.05	0.17
90°	674	245	69	0.39	1208	0.97		
45°	675	243	72	0.38	1165	1.41		

Barlat's (1991) coefficient —  $M = 8$ ,  $C_1 = 0.921$ ,  $C_2 = 1.095$ ,  $C_3 = 0.898$ ,  $C_6 = 1.031$ . Where,  $M$  = Exponent used in Barlat's anisotropic yield function, and  $C_{(1-6)}$  = material co-efficient of Barlat's anisotropic yield function.

YS = yield stress, UTS = ultimate tensile strength,  $n$  = strain hardening exponent,  $K$  = Strength coefficient,  $\bar{r}$  = plastic strain ratio (width vs. thickness strain),  $r$  = normal anisotropy,  $\Delta r$  = planer anisotropy. Direction 0°, 90° and 45° are angle with rolling direction of the sheets

**Table 4** Selected samples from experimental FLD

Strain	Effective Strain			Plane strain (PS)			Biaxial Strain (BS)		
	Uniaxial strain (US)	AISI 316L	AISI 304L	AA1050	AISI 316L	AISI 304L	AA1050	AISI 316L	AISI 304L
LS	0.20	0.22	0.14	0.20	0.23	0.16	0.21	0.29	0.19
IS	0.32	0.29	0.26	0.32	0.34	0.22	0.30	0.40	0.29
HS	0.46	0.46	0.34	0.38	0.50	0.31	0.45	0.58	0.42

Strains: low (*LS*), intermediate (*IS*) and high (*HS*). Strain paths: uniaxial (*US*), plane strain (*PS*) and biaxial (*BS*). The values of major, minor and effective strains are listed

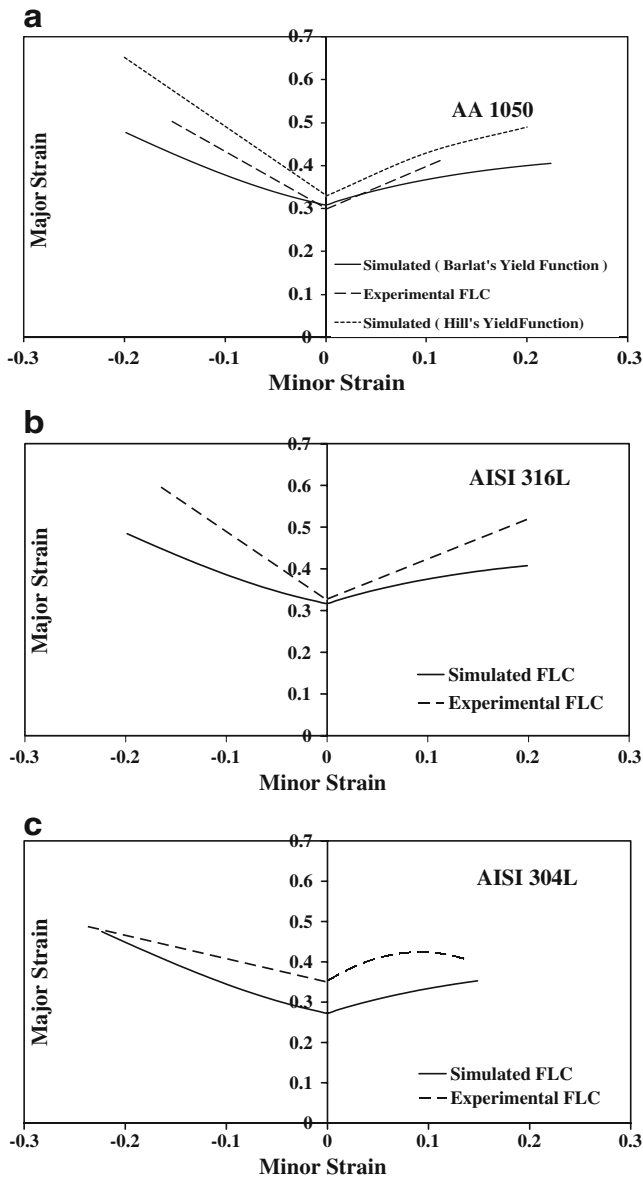


**Fig. 1** Comparison between experimental and simulated (with constant  $n$  and  $\bar{\sigma}$ ) FLCs for (a) AA 1050 using Barlat's 1991 and Hill's 48 yield criteria, (b) 316L using Hill's 48 yield criteria and (c) 304L Hill's 48 yield criteria

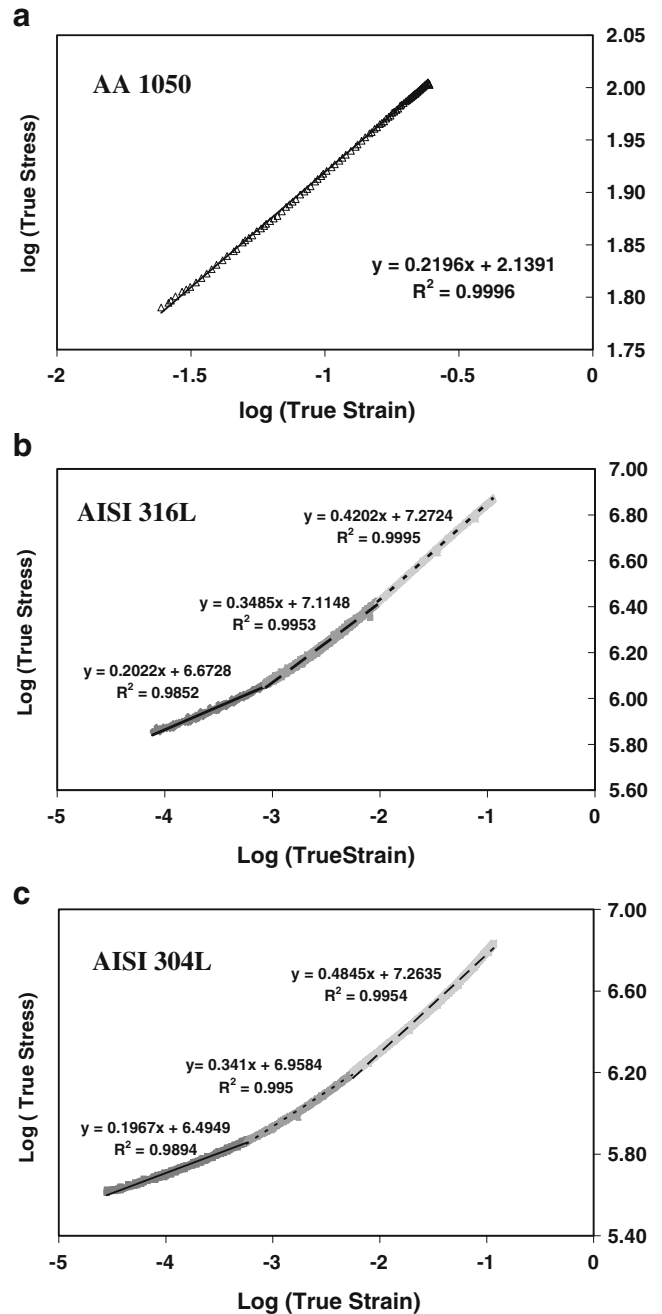


**Fig. 2** Plots of log (true stress) vs. log (true strain) for (a) AA 1050, (b) 316L and (c) 304L. The data were taken from standard tensile tests. From slope(s) of the plots,  $n$  value(s) were estimated

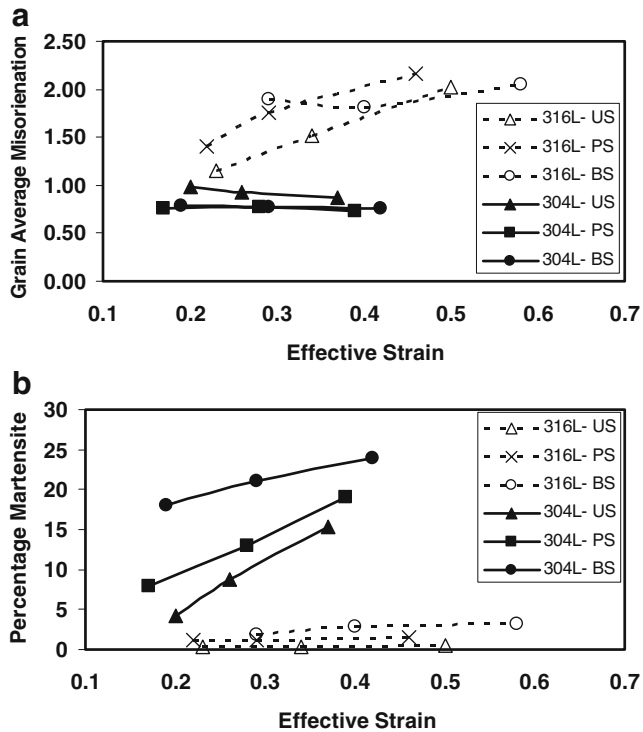


**Fig. 3** (a) Plots of grain average misorientation and effective strain for 316L and 304L. (b) Plots of percentage martensite and effective strain for 316L and 304L. Plots of normal anisotropy and effective strain

FLCs using varying material parameters

*Approximating changes in n variations and its role in FLC predictability*

In order to explore whether varying n can contribute to any improvement in FLC predictability, the first step required was to approximate changes in n with strain and strain path. During tensile tests, variations in n could be identified as a function of true or effective strain (Fig. 2). As shown in Fig. 2a, n did not change noticeably in AA1050, while significant variations were noted for 316L and 304L (Fig. 2b & c). As AA 1050 maintained almost constant n during tensile tests, it has been assumed that n values will

**Table 5** Grain average misorientation (GAM) in 316L and 304L

	Uniaxial		Plane Strain		Biaxial	
Strain	316L SS	304L SS	316L SS	304L SS	316L SS	304L SS
LS	1.15	0.98	1.41	0.76	1.89	0.79
IS	1.51	0.93	1.85	0.77	1.81	0.77
HS	2.02	0.87	2.16	0.73	2.05	0.76

Selected samples, for which grain average misorientation (GAM) values were measured, are listed in Table 4

**Table 6** Percentage Martensite in 316L and 304 L

	Uniaxial		Plane Strain		Biaxial	
Strain	316L SS	304L SS	316L SS	304L SS	316L SS	304L SS
LS	1.2	4.2	1.3	8	1.8	18
IS	1.2	9.1	1.4	11	2.9	21
HS	1.5	15.4	2.9	19	3.2	24

In 316L martensite percentage was measured from EBSD, while X-ray diffraction was used to quantify martensite in 304L. Selected samples, for which martensite percentages were measured, are listed in Table 3

not change during deformation and will remain constant for all the strain paths during simulation. The change in n for 316L and 304L can be linked to the development of microstructural features during deformation. It is assumed that the development in n will be scaled with two important microstructural features (i) Grain Average Misorientation (GAM) (ii) Strain Induced Martensite Formation (SIMF).

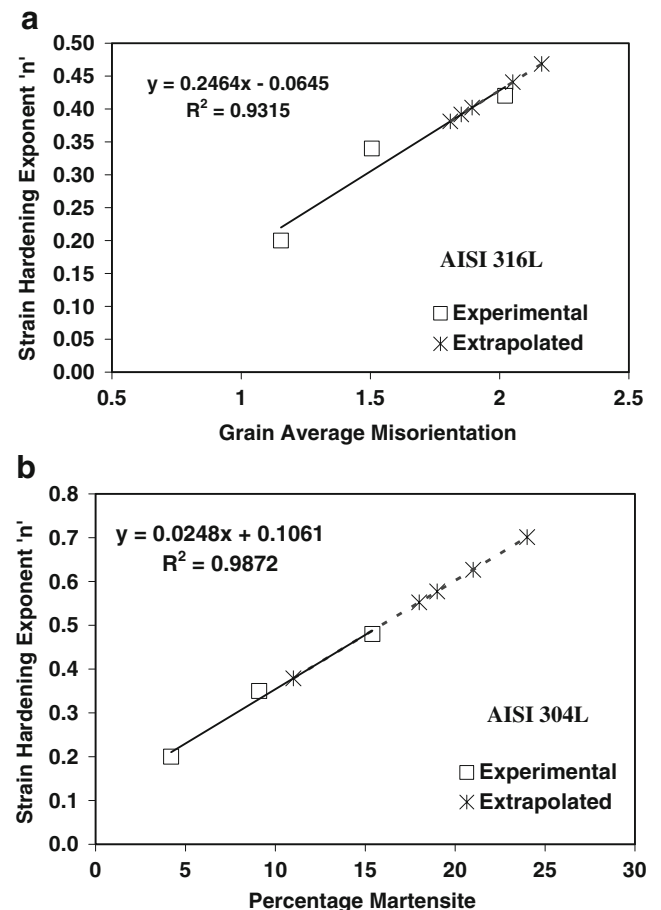


**Fig. 4** Extrapolation of Strain hardening exponent n. (a) n vs. grain average misorientation (GAM) in 316L and (b) n vs. percentage martensite in 304L. Experimental n values (where n values were obtained from Figs. 2b & c) were fitted in a linear function. n values for plane strain and biaxial strain-paths were then estimated from the linear function

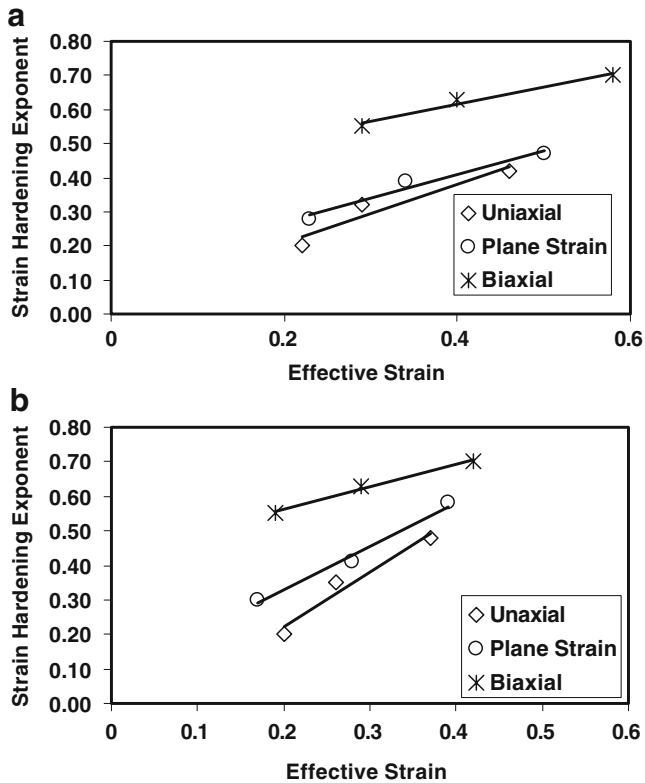


**Fig. 5** Plots of strain hardening exponent and effective strain (a) 316L and (b) 304L. For (a) & (b) the data were taken from standard tensile tests for uniaxial strain path and for plane strain & biaxial strain path data were taken from extrapolation of the data as in Fig. 3

As shown in Fig. 3a and Table 5, the GAM developments with effective strain in 316L are significant and strain path dependent but the change in 304L is very marginal. However, Fig. 3b and Table 6 shows that the formation of strain induced martensite is too insignificant for 316L. Therefore, in the absence of significant strain induced martensite formation,  $n$  will scale with GAM (as given in Table 5.) for 316L. In 304L, on the other hand, it was assumed that  $n$  will scale with the percentage strain induced martensite, as the formation of strain induced martensite is significant and strain path dependent. It may be noted that in 304 L sheets, GAM variations did not show any significant trend.

Trends in  $n$  were available (Fig. 2b & c) for 316L and 304L, but only for uniaxial strain path and limited range of effective strain. However, for *accurate* FLD estimation it is necessary to have variation in  $n$  for all the strain paths. To extend the range further<sup>4</sup>, assumptions were needed. As discussed in the previous section, the development in GAM for 316L (Fig. 3a and Table 5) and strain induced martensite for 304L (Fig. 3b and Table 6) is strain path dependent. The changes in GAM and percentage strain

<sup>4</sup> i.e. to cover other strain paths.

induced martensite were further plotted with experimental  $n$  values for uniaxial strain path and extrapolated for the other two strain paths (Fig. 4a & b). From such plots, straight linear relations were estimated. The relations were then extended to estimate  $n$  values (at intervals of 0.1 effective strains) for the other strain-paths (as shown in Fig. 5a & b). These were then used to conduct FE simulations with varying  $n$  (Fig. 6).

#### Possible changes in $\bar{r}$ and its implications for FLC predictability

Crystallographic texture was affected by strain and strain path — see Fig. 7 and Table 7. From the crystallographic texture, and using the standard fcc slip systems, the  $\bar{r}$  values were estimated [40–42] in AA1050 — see Table 8.  $\bar{r}$  vs. effective strain plots at three different strain paths yielded linear fit as shown in Fig. 8. The latter was then incorporated for varying  $\bar{r}$  estimates (at intervals of 0.1 effective strain) — to be implemented into FLC simulations. The FLC prediction incorporating  $\bar{r}$  evolution is shown in Fig. 9. It is clear from Fig. 9 that in AA1050, FLC predictability shows a clear, though numerically marginal, improvement — on both tensile and stretching sides.

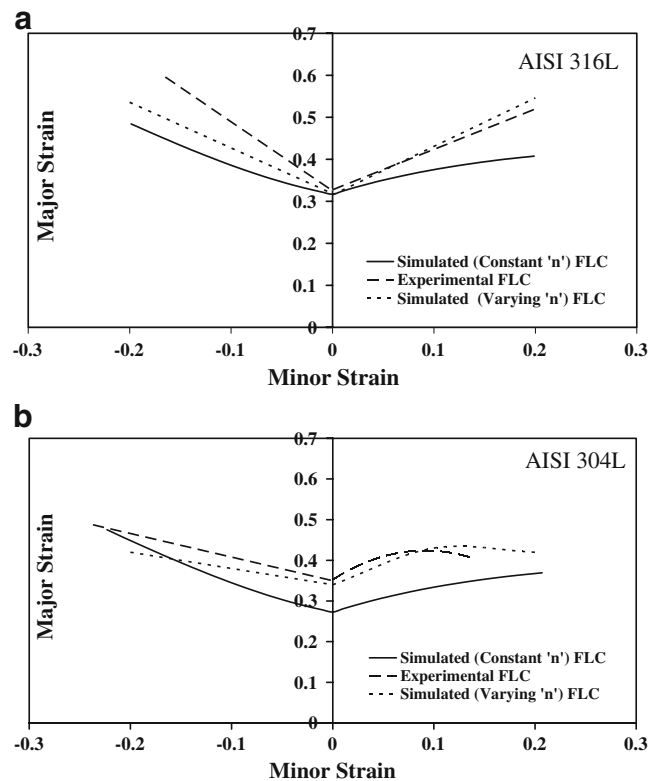


**Fig. 6** Comparison of experimental, FEM Calculated and FEM Calculated varying 'n' Forming limit diagram FLDs for (a) 316L SS and (b) 304L SS

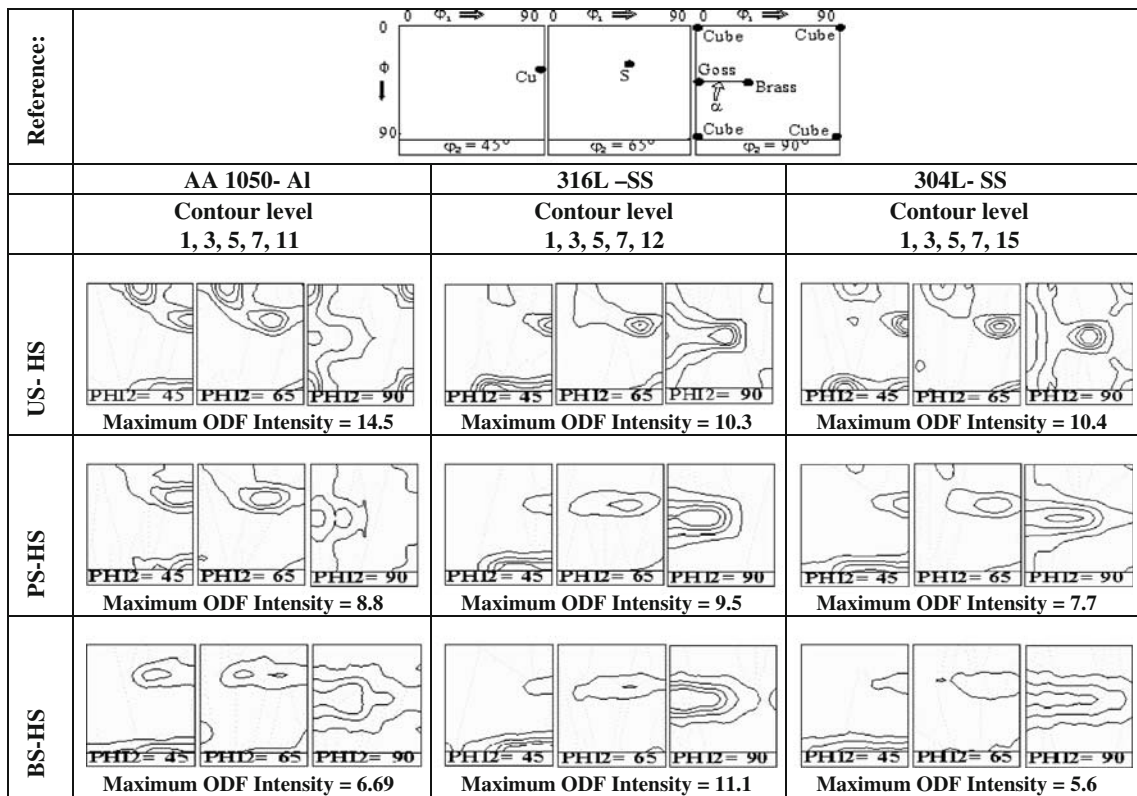


Fig. 7 X-ray ODFs, for  $\phi_2 = 45^\circ, 65^\circ$  &  $90^\circ$  sections, for the high strain (HS — see Table 4) state of all three strain paths and materials. The reference section, outlining ideal [47] orientations, is also included

Table 7 Texture index [40] for all three materials — after deformation at different strains and strain-paths (as in Table 3)

	Uniaxial			Plane Strain			Biaxial		
Strain	AA-1050	316L-SS	304L-SS	AA-1050	316L-SS	304L-SS	AA-1050	316L-SS	304L-SS
LS	3.95	3.214	2.88	4.8	3.664	2.468	4.14	3.865	2.566
IS	3.91	3.256	3.636	3.67	3.505	2.326	3.39	3.418	2.655
HS	3.82	3.739	3.887	3.60	3.656	3.305	2.66	3.668	2.457

Table 8 Texture estimated [40]  $\bar{r}$  values for the selected (as in table 4) samples of AA1050

Strain	Uniaxial	Plane strain	Biaxial
LS	1.34	1.43	0.913
IS	1.38	0.97	0.833
HS	1.49	0.89	0.733

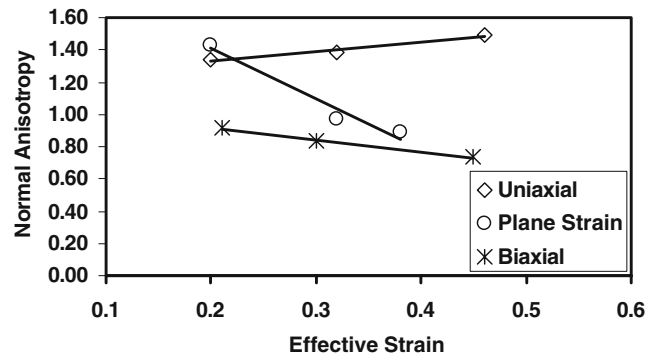
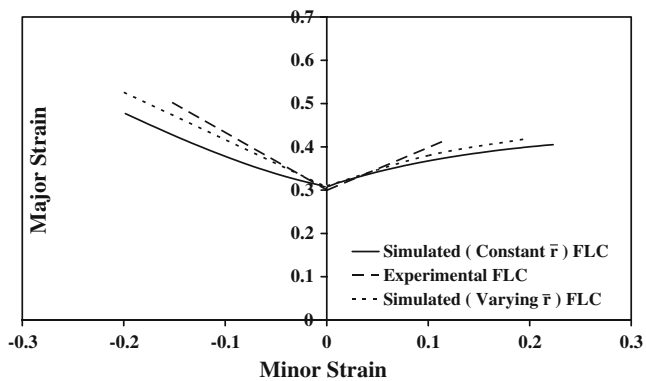


Fig. 8 Plots of normal anisotropy ( $\bar{r}$ ) and effective strain. For selected samples  $\bar{r}$  were estimated using texture estimated data [40] as in Table 8



**Fig. 9** Comparison of experimental and simulated FLCs of AA1050. FLC simulations were conducted taking constant and varying  $r$ . Variations in texture estimated  $r$  values, as used in the simulation, are listed in Table 8

Figure 6 clearly shows the effectiveness of using varying  $n$  towards improvements in FLC predictability. The match was almost perfect in the biaxial side (for both grades), though on the uniaxial side differences did still exist. However, improvements in FLC predictability may also be obtained by incorporating varying  $\bar{r}$  in 316L and 304L. Austenitic stainless steels can have significant twinning [34] and strain induced martensite formations [35–38] and therefore there is no simple procedure to estimate  $\bar{r}$  from microstructure and crystallographic texture and this is not in the scope of the present work.

## Discussion

The microstructure represents size-shape-orientation of grains, phases and defects [49]. It has significant impact on many different properties, especially those sensitive to microstructure [49]. Sheet metal formability strongly depends on the microstructure [31, 35–36]. Formability also has significant technical and commercial implications. As yet, relating exact microstructural inputs for formability predictions remains at best a ‘qualitative’ subject. The reason for this is the limited ability to translate different aspects of microstructure into quantitative numbers of material properties affecting formability. It is this factor which provided the impetus and motivation for the present study.

The present study used the FE analysis approach and suitable yield criteria (Barlat for AA1050 and Quadratic Hill for 316L & 304L) to predict FLCs. This was attempted using both constant and varying  $\bar{r}$  and  $n$ . A few interesting past studies can be cited [31–32], where varying  $\bar{r}$  and  $n$  (from actual mechanical test data) were used successfully for improved FLC predictions. Past studies [34–36] have also shown a strong correlation between microstructure with strain and strain path. However, what makes the

present study interesting is that it could convert tangible aspects of microstructural developments (e.g. developments in in-grain misorientation, strain induced martensite formation and crystallographic texture) into quantitative numbers of microstructure-sensitive properties — namely  $\bar{r}$  and  $n$ . These were then used successfully for better FLC predictability (Figs. 6 and 9).

This study is an initial attempt to highlight the possibility of using direct microstructural inputs towards better formability analysis. Unquestionably, such efforts need to be even more quantitative and with fewer ad-hoc assumptions, where complexities of microstructure and of microstructural developments can be effectively related to suitable anisotropic yield criteria and to strain path dependent hardening laws.

## Summary

Experimental and simulated (using Finite Element analysis) FLCs (forming limit curve) were generated for AA1050 and AISI 316L & 304L. The simulations were conducted using both constant and varying continuum material properties (namely  $\bar{r}$  and  $n$ ).

- In AA1050, the use of varying  $\bar{r}$  could improve FLC predictability. ( $\bar{r}$  estimates were obtained from crystallographic texture). The improvement was clear, though numerically marginal.
- Variations in  $n$  were estimated experimentally from tensile tests. These were then related to in-grain misorientation developments in 316L and to percentage strain induced martensite in 304L. This procedure allowed extending  $n$  estimates to different levels of strains and strain paths. Incorporating varying  $n$  did cause significant improvement in FLC predictability, especially on the biaxial side of 316L and 304L FLCs.

This study brings out clear possibilities for using direct microstructural inputs towards better FLC predictability.

**Acknowledgement** The authors would like to acknowledge financial support from IFCPAR/CEFIPRA (Indo-French Centre for the Promotion of Advanced Research) & DST (Department of Science & Technology) and the texture and microtexture measurements at the National Facility of Texture & OIM (a DST-IRPHA facility) at IIT Bombay.

## References

1. Keeler SP (1965) Determination of forming limits in automotive stampings. *Sheet Metal Industries* 42:683–691
2. Goodwin GM (1968) Application of strain analysis to sheet metal forming problems in the press shop. *Trans SAE* 77:380–387
3. Hecker SS (1975) Simple technique for determining forming limit curves. *Sheet Metal Industries* 58:671–676

4. Hosford WF, Duncan JL (1999) Sheet metal forming: A review. *Journal of Metals* 51:39–44
5. Lu ZH, Lee D (1987) Prediction of history-dependent forming limits by applying different hardening models. *Int J Mech Sci* 29:123–137
6. Nakamachi E (1995) Sheet-forming process characterization by static-explicit anisotropic elastic-plastic finite-element simulation. *J Mat Proc Tech* 50:116–132
7. Yoshida T, Kayayama T, Usuda M (1995) Forming-limit analysis of hemispherical-punch stretching using the three-dimensional finite-element method. *J Mat Proc Tech* 50:226–237
8. Takuda H, Mori K, Takakura N, Yamaguchi K (2000) Finite element analysis of limit strains in biaxial stretching of sheet metals allowing for ductile fracture. *Int J Mech Sci* 42:785–798
9. Tourki Z, Zegloul A, Ferron G (1996) Sheet metal forming simulations using a new model for orthotropic plasticity. *Comp Mater Sci* 5:255–262
10. Uthaisangskuk V, Prah U, Munstermann S, Bleck W (2008) Experimental and numerical failure criterion for formability prediction in sheet metal forming. *Comp Mater Sci* 43:43–50
11. Shena W, Penga LH, Tang CY (2005) An anisotropic damage-based plastic yield criterion and its application to analysis of metal forming process. *Int J Mech Sci* 47:1897–1922
12. Wang L, Lee TC (2006) The effect of yield criteria on the forming limit curve prediction and the deep drawing process simulation. *Int J Machine Tools & Manuf* 46:988–995
13. Cao J, Yao H, Karallis A, Boyce MC (2000) A predictive tool for delaying wrinkling and tearing failure in sheet. *Int. J Plasticity* 16:1105–1129
14. Noori H, Mahmudi R (2007) Prediction of forming limit diagrams in sheet metals using different yield criteria. *Metall Mater Trans A* 38:2040–2052
15. Stoughton TB, Zhu X (2004) Review of theoretical models of the strain-based FLD and their relevance to the stress-based FLD. *Int J Plasticity* 20:1463–1486
16. Hill R (1948) A theory of yielding and plastic flow of anisotropic metals. *Proc Roy Soc London A* 193:281–297
17. Woodthorpe J, Pearce R (1970) The anomalous behavior of aluminum sheet under balanced biaxial tension. *Int J Mech Sci* 12:341–347
18. Cazacu O, Barlat F (2003) Application of representation theory to describe yielding of anisotropic aluminum alloys. *Int J Engg Sci* 41:1367–1385
19. Karafillis AP, Boyce MC (1993) A general anisotropic yield criterion using bounds and a transformation weighting tensor. *J Mechanics and Physics of Solids* 41:1859–1886
20. Barlat F, Brem JC, Yoon JW, Chung K, Dick RE, Lege DJ, Pourboghraat F, Choi SH, Chu E (2003) Plane stress yield function for aluminum alloy sheets. *Int J Plasticity* 19:1297–1319
21. Banabic D, Bunge HJ, Pohlandt K, Tekkaya AE (2000) Plastic anisotropy formability test forming limits. *Formability of Metallic Materials* (Editor: Banabic D) Springer Verlag, Berlin
22. Tseng AA (1990) Material characterization and finite element simulation for forming miniature metal parts. *Finite Elements in Analysis and Design* 6:251–265
23. Zhibing Z, Yuqi L, Ting D, Zhigang L (2008) Blank design and formability prediction of complicated progressive die stamping part using a multi-step unfolding method. *J Mat Proc Tech* 205:425–431
24. Wagener HW (1997) New developments in sheet metal forming: sheet materials, tools and machinery. *J Mat Proc Tech* 72:342–357
25. Hecker SS (1974) A Cup test for assessing stretchability. *Mech Eng Quart* 14:30–36
26. Chu CC (1984) A Three-dimensional model of anisotropic hardening in metals. *J Mech Phys Solids* 32:197–212
27. Sing WM, Rao KP (1995) Influence of material properties on sheet metal formability limits. *J Mat Proc Tech* 48:35–41
28. Toth LS, Hirsch J, Van Houtte P (1996) On the role of texture development in the forming limits of sheet metals. *Int J Mech Sci* 38:1117–1126
29. Kumar DR (2002) Formability analysis of extra-deep drawing steel. *J Mat Proc Tech* 130–131:31–41
30. Banabic D, Comsa S, Jurco P, Cosovici G, Paraiuanu L, Julean D (2004) FLD theoretical model using a new anisotropic yield criterion. *J Mat Proc Tech* 157–158:23–27
31. Tourki Z, Bargui H, Sidhom H (2005) The kinetic of induced martensitic formation and its effect on forming limit curves in the AISI 304 stainless steel. *J Mat Proc Tech* 166:330–336
32. Abedrabbo N, Pourboghraat F, Carsley J (2007) Forming of AA5182-O and AA5754-O at elevated temperatures using coupled thermo-mechanical finite element models. *Int J Plasticity* 23:841–875
33. Sevillano JG, Van-Houtte P, Aernoudt E (1980) Large strain work hardening and textures. *Prog Mater Sci* 25:69–112
34. Mishra SK, Narasimhan K, Samajdar I (2007) Deformation twinning in AISI 316L austenitic stainless steel - Role of strain and strain path. *Mater Sci Tech* 23:1118–1126
35. Hecker SS, Stout MG, Staudhammer KP, Smith JL (1982) Effects of strain state and strain rate on deformation-induced transformation in 304 stainless steel—1. Magnetic measurements and mechanical behavior. *Metall Trans A* 13:619–626
36. Perdahcioglu ES, Geijselaers JGM, Huetink J (2008) Influence of stress state and strain path on deformation induced martensitic transformations. *Mater Sci Engg A* 481–482:727–731
37. Wasnik DN, Gopalkrishnan IK, Yakhami JV, Kain V, Samajdar I (2003) Cold rolled texture and microstructure in types 304 and 316L austenitic stainless steels. *Iron and steel Institute of Japan International* 43:1581–1589
38. Wasnik DN, Kain V, Samajdar I, Verlinden B, De PK (2003) Resistance to sensitization and intergranular corrosion through extreme randomization of grain boundaries. *Acta Mater* 49:4587–4601
39. Barlat F, Lege DJ, Brem JC (1991) A six-component yield function for anisotropic materials. *Int. J. Plast.* 7:693–712
40. Van-Houtte P (1995) *MTM-FHM Software Manual*. Katholieke Universiteit Leuven, Belgium
41. Bunge HJ (1982) *Texture Analysis in Materials Science*. Butterworth, London (1982)
42. Van Houtte P (1987) Calculation of Yield Locus of Textured Polycrystals using the Taylor and the relaxed Taylor Theory. *Textures and Microstructures* 7:29–72
43. Yerra SK, Verlinden B, Van-Houtte P (2005) On crystallographic texture of as-drawn doped-W wires. *Mater Sci Forum* 495–497:913–918
44. Geroult E (1999) Bainitic transformation in TRIP- Assisted steels and its influence on mechanical properties. Ph. D Thesis. Department MTM, Katholieke Universiteit Leuven, Belgium
45. Samajdar I, Doherty RD (1998) Cube recrystallization texture in warm deformed aluminum. *Acta Mater* 46:3145–3158 Z
46. Marciniak Z, Kuczynski K (1967) Limit strain in the processes of stretch forming sheet metal. *International Journal of Mechanical Sciences* 9:609
47. Nandedkar VM, Narasimhan K (1999) Measurement of strain history during the stretching of forming-grade steel sheets. *J Mater Proc Tech* 89–90:24–29
48. Kumar S, Date PP, Narasimhan K (1994) A new criterion to predict necking failure under biaxial stretching. *J Mater Proc Tech* 45:583–588
49. Verlinden B, Driver J, Samajdar I, Doherty RD (2007) *Thermo-Mechanical Processing of Metallic Materials*, ISBN-978-0-08-044497-0, Pergamon Materials Series - series. Cahn RW (ed). Elsevier, Amsterdam